Journal of
Materials Chemistry C

ROYAL SOCIETY OF CHEMISTRY

PAPER

View Article Online
View Journal | View Issue

Published on 15 March 2022. Downloaded by HeFei University of Technology on 4/23/2022 1:15:50 AM.

Cite this: *J. Mater. Chem. C*, 2022, **10**, 6025

A quasi-2D perovskite antireflection coating to boost the performance of multilayered $PdTe_2$/Ge heterostructure-based near-infrared photodetectors†

Huahan Chen,[a] Chao Xie, *[b] Xianpeng Zhong,[a] Yi Liang,[a] Wenhua Yang,[b] Chunyan Wu [a] and Linbao Luo *[a]

A hybrid heterostructure composed of two-dimensional (2D) material/narrow bandgap semiconductor represents a promising platform for designing highly efficient and cost-effective near-infrared (NIR) photodetectors. However, performance enhancement is usually restricted by reduced light usage due to relatively high refractive indexes and low absorption coefficients of the hybrid heterostructures. Herein, we demonstrate that a quasi-2D perovskite thin film can serve well as an antireflection coating to greatly boost the performance of a multilayered $PdTe_2$/Ge heterostructure-based NIR photodetector. Specifically, upon the perovskite coating with an optimized thickness, photoresponsivity and specific detectivity can be improved significantly from $\sim$526.4 mA W^{-1} to $\sim$976.2 mA W^{-1} and from $\sim 2.43 \times 10^{11}$ Jones to $\sim 4.78 \times 10^{11}$ Jones, respectively, under a 1550 nm optical communication wavelength with a light intensity of $\sim$70 μW cm^{-2} at zero bias. Meanwhile, other important performance parameters including dark current and response speed can maintain almost identical. Moreover, owing to the improved moisture resistance of the upper quasi-2D perovskite layer, the photodetector exhibits excellent device stability and operational durability under atmospheric conditions. The results not only provide a convenient route for improving the performance of NIR optoelectronic devices but also broaden the application scope of perovskite materials.

Received 30th January 2022,
Accepted 14th March 2022

DOI: 10.1039/d2tc00438k

rsc.li/materials-c

Introduction

Photodetectors operating in the near-infrared (NIR, typically refers to light irradiation in the wavelength range of 780–3000 nm) wavelength regime are critical components of a series of electronic and optoelectronic devices including night vision reviewer, laser rangefinder, optical communication system, infrared digital camera, remote sensing imaging system and medical diagnostics apparatus.[1–4] Commercial NIR photodetectors are usually composed of traditional inorganic semiconductors, *e.g.* bulk crystalline Si, Si/Ge heterostructures, III–V semiconductors and related alloys.[5,6] While they have indeed achieved outstanding photoresponse characteristics in the NIR wavelength region, dilemmas such as strictly required high-quality epitaxially grown photosensitive materials, complicated device geometries, complex multistep manufacturing procedures, high-vacuum and expensive instruments make these NIR photodetectors uneconomical, which prevents their extensive usage as well.[5] Such a predicament has prompted researchers to seek for alternative solutions for the development of high-performance cost-effective NIR photodetectors. In recent years, there has been great interest in exploring optoelectronic devices based on emerging two-dimensional (2D) layered material/three-dimensional (3D) traditional semiconductor hybrid heterostructures.[7–10] In these heterostructures, the 3D semiconductor usually acts as the primary optical absorbing media to generate photocarriers, whereas the 2D layered material serving as an active layer is employed to separate and transport photocarriers. Simple device geometries and ease of manufacturing render 2D/3D hybrid heterostructures extremely promising for constructing optoelectronic devices with low cost. In addition, they are often characterized by the following advantages as well: (1) enhanced photon absorption efficiency and broadened photon absorption spectral range, (2) accelerated separation and transport of photocarriers assisted by a built-in electric field and (3) exotic functionalities enabled by the complementary characteristics of two components.

[a] School of Microelectronics, Hefei University of Technology, Hefei, Anhui 230009, P. R. China. E-mail: luolb@hfut.edu.cn

[b] Information Materials and Intelligent Sensing Laboratory of Anhui Province, Industry-Education-Research Institute of Advanced Materials and Technology for Integrated Circuits, School of Electronics and Information Engineering, Anhui University, Hefei, Anhui 230601, P. R. China. E-mail: chaoxie@ahu.edu.cn

† Electronic supplementary information (ESI) available. See DOI: 10.1039/d2tc00438k

Published on 15 March 2022. Downloaded by HeFei University of Technology on 4/23/2022 1:15:50 AM.

By selecting 3D semiconductors with a narrow bandgap, such as Ge, NIR photodetectors based on 2D/3D hybrid heterostructures with respectable performance have been realized recently.[11,12] For example, Zeng *et al.* first designed a NIR photodetector based on a graphene/planar Ge heterostructure, which has responsivity and specific detectivity values of 51.8 mA W^{-1} and 1.38×10^{10} Jones, respectively, under 1550 nm light irradiation.[13] By transferring a multilayered $PtSe_2$ film atop a Ge substrate, Wang and colleagues reported a NIR photodetector with a responsivity attaining 602 mA W^{-1}.[14] In spite of the progresses, further performance improvement has been impeded by the relatively low barrier height of the heterostructures and/or insufficient usage of incident photons due to the high NIR light reflection of the planar geometry because of a relatively high refractive index and a low absorption coefficient of the Ge material. To address these difficulties, some different strategies have been proposed. For instance, by employing an additional top transparent gate to regulate the barrier height of a graphene/Ge heterostructure, the responsivity can be enhanced drastically to ~750 mA W^{-1}, however, at the expense of low energy consumption.[15] Another strategy to increase the NIR light usage is exploiting the light trapping effect by creating nanostructures on the Ge substrate or introducing plasmonic nanostructures resonated at the NIR regime. Lu *et al.* modified plasmonic tin-doped indium oxide (ITO) nanoparticles atop a graphene/Ge nanoneedle array, which enhances the responsivity to ~185 mA W^{-1}.[16] A NIR photodetector comprising a $PdSe_2$ multilayer atop a Ge nanocone array has also been presented, demonstrating a responsivity of 530.2 mA W^{-1}.[17] However, it should be emphasized that, although this strategy can significantly promote the incident light absorption, the etching of Ge may reduce the conformal contact between 2D and 3D components, which weakens the charge separation at the junction interface and is therefore unfavorable for performance enhancement. The etching and additional modification processes also increase the complexity and uncontrollability during device fabrication, which reduces reproducibility of the NIR photodetectors. In addition to the above introduced strategies, light trapping with an antireflection coating (ARC) may be another effective tactic that can abstain the shortcomings of light trapping with nanostructures.[18,19] Nevertheless, to date, this strategy has rarely been explored on 2D/3D hybrid heterostructure-based NIR photodetectors.

In this work, we present that the performance of a multilayered $PdTe_2$/Ge 2D/3D heterostructure-based NIR photodetector can be greatly boosted with an ARC of a quasi-2D perovskite thin film, a representative of the perovskite family featuring excellent intrinsic chemical stability and photostability that have recently shown great promise in photovoltaic and photodetection applications.[20,21] By optimizing the thickness of the perovskite ARC, the device performance parameters in terms of photocurrent responsivity and specific detectivity are almost doubled while other parameters including dark current and response speed can keep nearly unchanged. Such an enhancement is directly related to the pronounced NIR light trapping effect of the quasi-2D perovskite ARC, according to the theoretical simulation based on the finite element method. A typical NIR photodetector with the perovskite ARC demonstrates a high responsivity of ~976.2 mA W^{-1}, a decent specific detectivity of ~4.78×10^{11} Jones, and a fast response speed of 35.9/40.7 μs, at zero bias under 1550 nm light irradiation. By further applying a reverse bias voltage of −1 V, the responsivity can be improved to as high as 1216.7 mA W^{-1}, corresponding to an external quantum efficiency exceeding 95%. In addition, thanks to the improved moisture resistance of the upper quasi-2D perovskite layer, the device performance can maintain ~96.3% after 30 days of storage under ambient conditions, showing superior air stability.

Results and discussion

Fig. 1(a) shows a schematic diagram of the multilayered $PdTe_2$/Ge 2D/3D heterostructure-based NIR photodetector with the quasi-2D perovskite ARC. The multilayered $PdTe_2$ film as a representative of group-10 transition metal dichalcogenide (TMD) was grown through thermal-assisted tellurization of a pre-deposited Pd film[22] and was transferred atop a planar Ge substrate covered with an insulating layer with a pre-defined open window. Then, a thin film of the quasi-2D perovskite was spin-coated on the top of the $PdTe_2$ layer to complete the construction of the NIR photodetector (Fig. S1, ESI†). The detailed procedures for device construction could be found in the Experimental section. Fig. 1(b) depicts the cross-sectional SEM image of an as-fabricated heterostructure device. Clearly, a double-layer stacked structure could be easily observed. The thicknesses of the $PdTe_2$ multilayer and quasi-2D perovskite were determined to be ~57 and ~190 nm, respectively. Fig. 1(c) show the SEM image of the as-synthesized $PdTe_2$ multilayer on a Si oxide substrate, showing a continuous, uniform and relatively flat film. Clearly, the observation found that the $PdTe_2$ multilayer was actually composed of substantial compact crystalline domains with sizes of about 100–450 nm (Fig. S2(a), ESI†), forming a typical polycrystalline structure, as further confirmed by the AFM image shown in Fig. 1(d). The thickness of the $PdTe_2$ layer derived from the ~8 nm Pd film was about ~58.8 nm with a root mean square roughness of ~6.67 nm, consistent with the result seen from the SEM image. The XRD pattern in Fig. 1(e) disclosed prominent diffraction peaks situated at 17.48°, 31.14°, 35.02° and 53.65°, which corresponded to (001), (101), (002) and (003) crystal planes of $PdTe_2$, respectively. No additional Pd peaks could be observed in the pattern, suggesting that the Pd precursor had been fully transformed into $PdTe_2$ with a high phase purity. In addition, as observed in Fig. 1(f), the Raman spectra collected from six random spots of the as-prepared sample showed a good consistency with all spectra consisting of two distinct vibrational modes at ~77.1 and ~135.8 cm^{-1}, which was due to the in-plane (E_g) and out of-plane (A_{1g}) motions of Te atoms, respectively.[23] Furthermore, 2D Raman mapping was conducted on the sample as displayed in Fig. 1(g), from which a rather narrow distribution of the A_{1g} active mode over a

 This journal is © The Royal Society of Chemistry 2022

Published on 15 March 2022. Downloaded by HeFei University of Technology on 4/23/2022 1:15:50 AM.

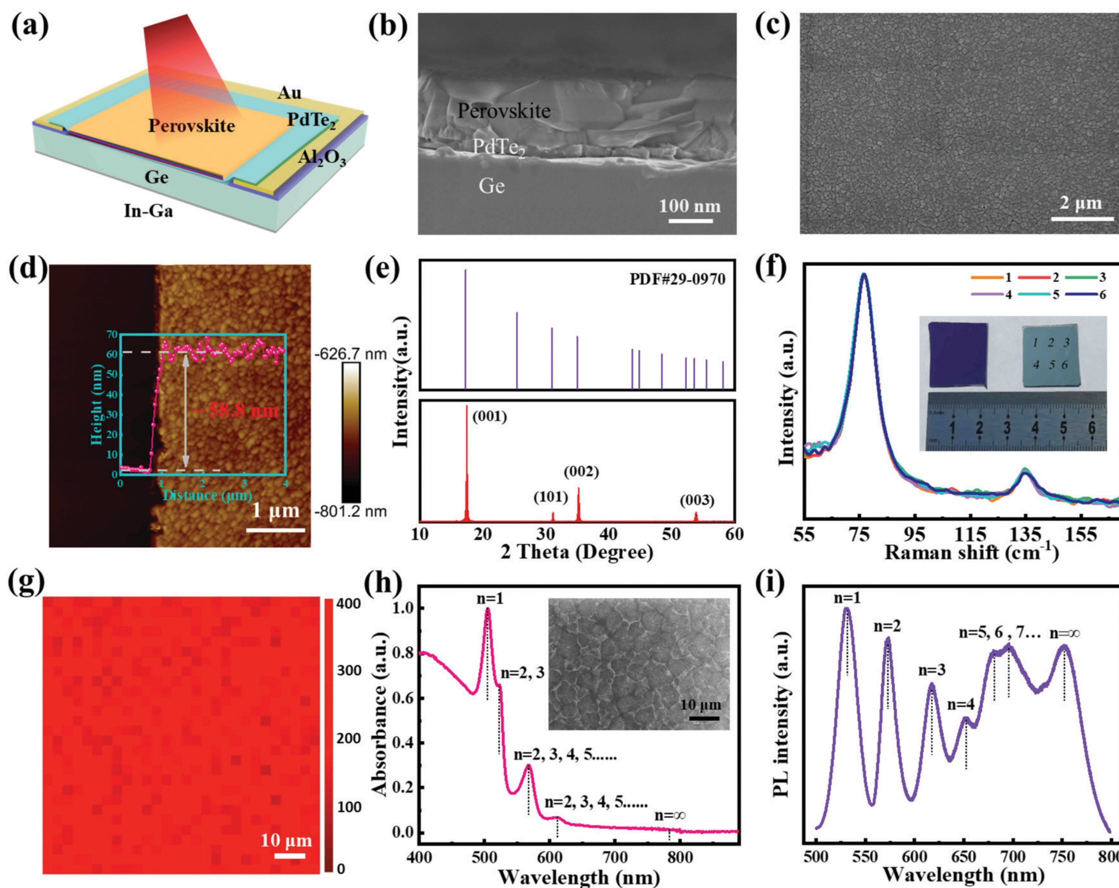

Fig. 1 (a) Schematic diagram of the $PdTe_2$/Ge 2D/3D heterostructure-based NIR photodetector with a quasi-2D perovskite ARC. (b) Cross-sectional SEM image of a $PdTe_2$/Ge 2D/3D heterostructure covered with a quasi-2D perovskite. (c) SEM image, (d) AFM image and (e) XRD pattern of the as-synthesized $PdTe_2$ layer. The inset in (d) shows the height profile. (f) Raman spectra of six random spots on the $PdTe_2$ layer. The inset in (f) shows the optical image containing a bare Si oxide substrate (left) and a Si oxide substrate covered with the $PdTe_2$ layer (right). (g) 2D Raman mapping of the $PdTe_2$ layer over 100×100 μm^2. (h) Absorbance spectrum and (i) PL spectrum of the quasi-2D perovskite film. The inset in (h) shows the SEM image of the as-prepared quasi-2D perovskite.

100×100 μm^2 area was found. The above results indicated that the $PdTe_2$ multilayer derived from the thermal-assisted tellurization technique had a high film quality with an excellent uniformity and homogeneity. The quasi-2D perovskite used here has a chemical formula of $(PEA)_2(MA)_{n-1}Pb_nI_{3n+1}$, where PEA^+ and MA^+ denote $C_8H_9NH_3^+$ and $CH_3NH_3^+$, respectively, and n represents the lead iodide octahedral layers between two PEA^+ organic spacers.[24] The film was prepared through a two-step ligand exchange technique described in a previous study,[25] which would render a quasi-2D perovskite with a composition gradient in the vertical direction, *e.g.*, the small-n and large-n perovskite phases accumulated close to the upper and bottom surfaces, respectively, in our study. Such a composition gradient was likely to result in a refractive index gradient in the quasi-2D perovskite, which might be advantageous to the antireflection effect. The inset in Fig. 1(h) depicts the top-view SEM image of the as-prepared quasi-2D perovskite film, showing a continuous and compact film with a grain size of several micrometers and no pinholes. The absorption spectrum of the quasi-2D perovskite film on a quartz substrate is shown in Fig. 1(h), where distinct absorption peaks at wavelengths of ~505, ~523, ~567, ~611 and ~782 nm could be attributed to $(PEA)_2(MA)_{n-1}Pb_nI_{3n+1}$ perovskites with $n = 1, 2, 3, 4, 5, \ldots, \infty$ (Fig. S2(b), ESI†). As displayed by the PL spectrum in Fig. 1(i), obvious emission peaks corresponding to the radiative recombination of $n = 1, 2, 3, 4, 5, 6, 7, \ldots, \infty$ perovskite phases were found, which was in agreement with previous studies.[26,27] The results combined with the observed refractive index gradient discussed later confirmed that the quasi-2D perovskite film with graded multiple phases was successfully prepared.

The electrical properties of the multilayered $PdTe_2$/Ge 2D/3D heterostructure with the quasi-2D perovskite ARC were first evaluated in the darkness. Fig. S3(a) (ESI†) compares the current–voltage (I–V) curves of a typical heterostructure before and after coating of the quasi-2D perovskite in the darkness. Obviously, the nearly identical I–V curves implied that the quasi-2D perovskite coating has a negligible influence on the electrical characteristics of the $PdTe_2$/Ge heterostructure. Fig. 2(a) plots the I–V curve of the heterostructure in both linear and semi-logarithmic scales, showing a pronounced rectifying behavior with a forward-to-reverse current ratio of $\sim 3.2 \times 10^2$ at ± 1 V. The high value was superior to many 2D/3D

View Article Online

Published on 15 March 2022. Downloaded by HeFei University of Technology on 4/23/2022 1:15:50 AM.

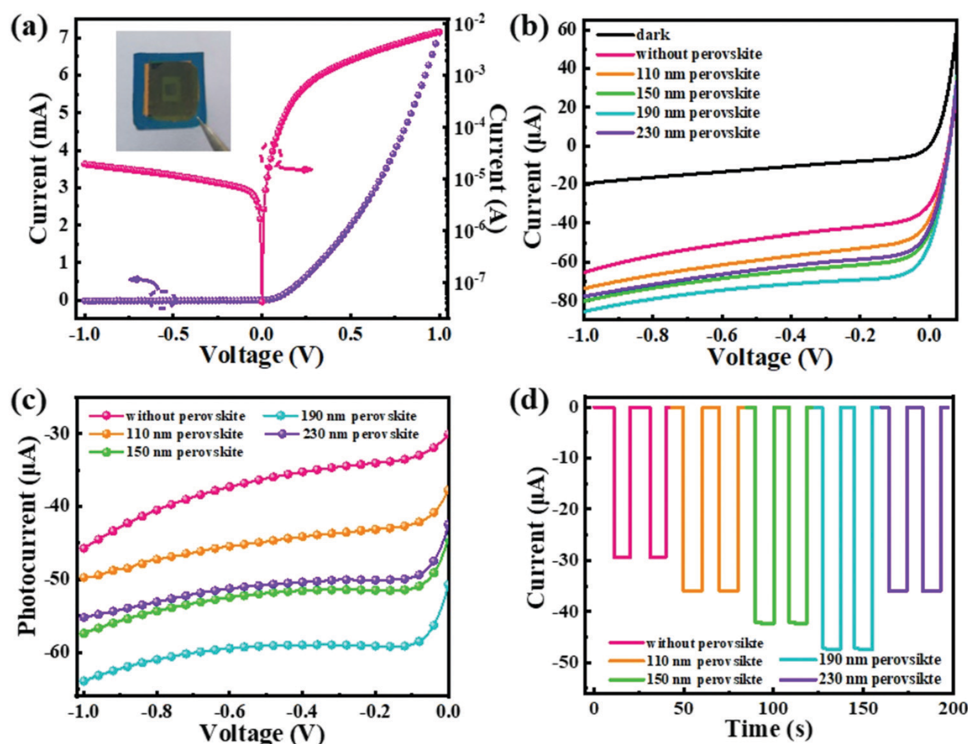

Fig. 2 (a) Dark I–V curves of the $PdTe_2$/Ge 2D/3D heterostructure in linear and logarithmic coordinates. The inset shows an optical image of the as-fabricated device. (b) I–V curves, (c) net photocurrent and (d) time-dependent photoresponses of the heterostructure photodetector with the perovskite ARC in different thicknesses under 1550 nm NIR light illumination at an intensity of ∼1379 μW cm^{-2}.

heterostructures in literature studies, including graphene/Ge (∼50), multilayered $PtSe_2$/Si (∼100) and multilayered $PdSe_2$/Ge (∼5).[13,28,29] In addition, by deducing the $\ln I$–V curve (Fig. S3(b), ESI†) following the equation: $n' = \frac{q}{k_B T}\frac{dV}{d\ln I}$, where q, k_B and T represent the elementary charge, Boltzmann's constant and Kelvin temperature, respectively, the ideality factor n' of the heterostructure was determined to be ∼1.41. The n' value was close to the ideal value of a diode (n' = 1), and smaller than many previously reported 2D/3D heterostructures, *e.g.* multilayered MoS_2/Si (n' = 1.83) and graphene/GaAs nanocones (n' = 3.25).[30,31] Furthermore, the barrier height of the $PdTe_2$/Ge heterostructure was calculated to be ∼677.4 meV (Fig. S3(c), ESI†), based on the thermionic emission theory.[32] Such a value was superior to graphene/Si (∼450 meV), multilayered MoS_2/Si (∼330 meV), and close to that of few-layered $PtSe_2$/Si (∼710 meV) 2D/3D heterostructures.[28,30,32] The generality of the above results suggested the high quality of the present $PdTe_2$/Ge 2D/3D heterostructure.

Next, the photoresponse properties of the multilayered $PdTe_2$/Ge heterostructure with the quasi-2D perovskite ARC were characterized under 1550 nm NIR light irradiation. Fig. 2(b) compares the I–V curves of the devices with the ARC in different thicknesses at a constant light intensity of ∼1379 μW cm^{-2}, compared with that in the darkness. Significantly, upon NIR light illumination, the heterostructure displayed a pronounced photovoltaic behavior with a short-circuit current of about 30.11 μA and an open-circuit voltage of about 54.99 mV, respectively, even without the quasi-2D perovskite ARC. Such an effect could enable the heterostructure to function as a self-driven NIR photodetector, which would reduce the energy consumption. In addition, it was found that with an increasing quasi-2D perovskite thickness from 0 nm (without the perovskite) to ∼190 nm (Fig. S4(a–c), ESI†), the photovoltaic effect became more noticeable gradually and the currents at both zero and reverse biases rose monotonously as well. Interestingly, further increasing the quasi-2D perovskite thickness to ∼230 nm (Fig. S4(d), ESI†) led to weakened photovoltaic activity and reduced current at both zero and reverse biases, compared to those for the device with the ∼190 nm-thick quasi-2D perovskite. The net photocurrent (I_{photo}) could be extracted by deducting the dark current (I_{dark}) from the current under light illumination (I_{light}): $I_{photo} = I_{light} - I_{dark}$. Fig. 2(c) displays the net photocurrent of the heterostructure device with the quasi-2D perovskite in various thicknesses at a bias voltage from −1.0 to 0 V. Remarkably, the net photocurrent at both zero and reverse biases exhibited the same evolution tendency, as shown in the I–V curves, for various thicknesses of the quasi-2D perovskite. Specifically, the values of the net photocurrent were about 30.06, 37.76, 44.31, 50.68 and 42.45 μA for the devices with the quasi-2D perovskite thicknesses of 0, ∼110, ∼150, ∼190 and ∼230 nm, respectively, at zero bias, and it had be improved by as high as ∼68.59% upon coating of the ∼190 nm-thick quasi-2D perovskite. Time-dependent photoresponse properties were further studied under periodically switched NIR light illumination, as shown in Fig. 2(d). Clearly, at different quasi-2D perovskite thicknesses, all devices could be reversibly and repeatedly turned between low- and

 This journal is © The Royal Society of Chemistry 2022

Published on 15 March 2022. Downloaded by HeFei University of Technology on 4/23/2022 1:15:50 AM.

high-current statuses, showing excellent photo-switching features. The I_{light}/I_{dark} ratio attained 1.15×10^3 for the device with the ~190 nm-thick quasi-2D perovskite ARC. In addition, all time-dependent photoresponse curves exhibited steep rise and fall edges, implying quick separation and collection of photoexcited carriers in the heterostructures as well as fast response speeds of the NIR photodetectors.

The above intriguing photoresponse characteristics could be related to the pronounced light trapping capability of the quasi-2D perovskite thin layer at the NIR wavelength regime. Considering the high refractive index (n_g: ~4.0 for Ge, and n_t: ~3.11 for $PdTe_2$ layer, Fig. S5, ESI†) and low absorption coefficient of the Ge material,[33,34] a considerable part of incident NIR light would be reflected from the planar $PdTe_2$/Ge surface, which reduced the effective usage of incident NIR photons and was undesirable in high-performance Ge-based NIR photodetectors. In contrast, the quasi-2D perovskite film possessed a relatively lower refractive index (n_p: ~2.0 at 1550 nm), which was between Ge (n_g: ~4.0) and air (n_{air}: ~1.0) approximately correlated by $n_p = \sqrt{n_g n_{air}}$.[35] As shown in Fig. S5 (ESI†), the present quasi-2D perovskite film in fact had a slightly graded refractive index values of ~1.92 and ~2.03 at 1550 nm for the upper and bottom surfaces, respectively, due to the composition gradient in its vertical direction. Therefore, such a layer could effectively bridge the refractive disparity between the $PdTe_2$/Ge active layer and air, rendering the pronounced light–matter interaction.[36] Meanwhile, the quasi-2D perovskite with outstanding intrinsic chemical stability and photostability had a large bandgap greater than 1.5 eV, making it transparent at the NIR wavelength regime.[37] These features thus empowered the quasi-2D perovskite with an excellent antireflection effect for Ge-based NIR photodetectors.

Fig. 3(a) schematically shows the mechanism of light trapping with the antireflection effect of the quasi-2D perovskite film on the $PdTe_2$/Ge 2D/3D heterostructure. Because of the refractive disparity between air, quasi-2D perovskite, $PdTe_2$/Ge active layer, partial of the incident NIR light was reflected off the heterostructure, and the remaining was absorbed by the heterostructure to generate the photocurrent. The reflected part was determined by the thickness of the quasi-2D perovskite film and the wavelength of the incident NIR light, following the fundamental principles of optics.[38] To clearly elucidate the role of the quasi-2D perovskite ARC, we then performed a theoretical calculation to correlate the relationship between the optical absorption of the heterostructure and the thickness of the quasi-2D perovskite. As displayed in Fig. 3(b), the $PdTe_2$/Ge heterostructure could only absorb ~54.8% of the incident light at 1550 nm without the ARC. The value became stronger when coating a layer of the quasi-2D perovskite, and it rose gradually as the perovskite thickness increased, reaching a maximum absorption of ~88.6% at the

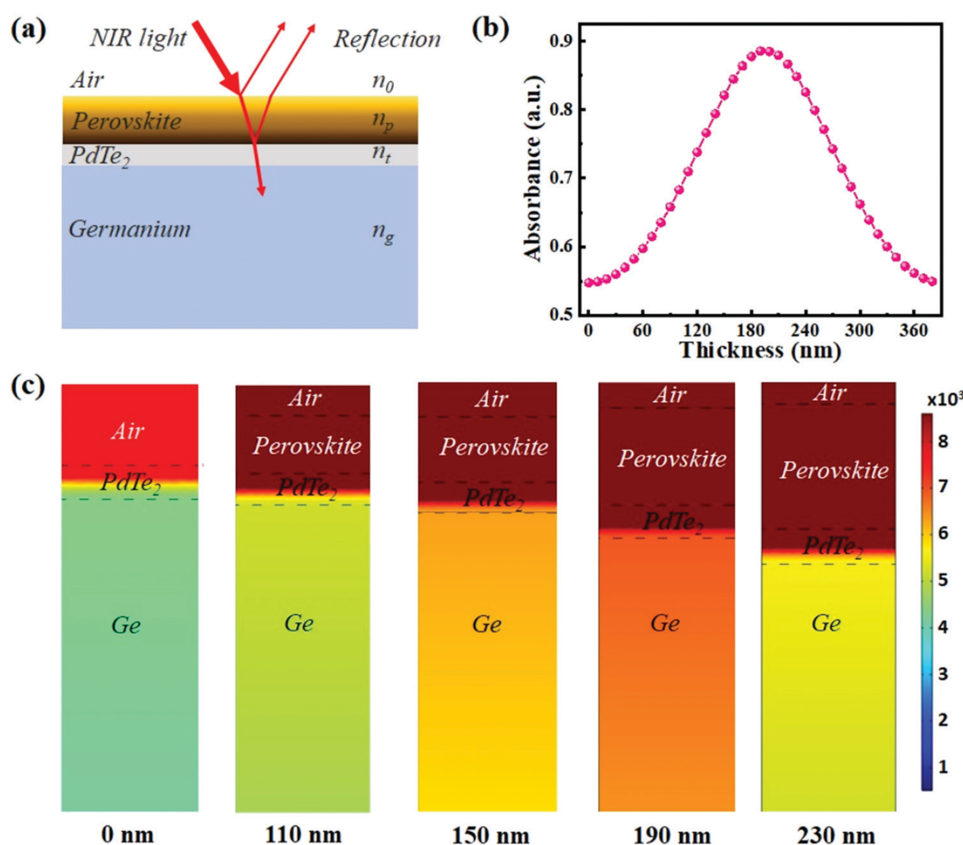

Fig. 3 (a) Schematic diagram showing the mechanism of light trapping with an antireflection effect of the quasi-2D perovskite layer on the $PdTe_2$/Ge 2D/3D heterostructure. (b) Simulated absorbance of 1550 nm NIR light illumination as a function of the quasi-2D perovskite thickness. (c) The electric field distribution of the $PdTe_2$/Ge heterostructure covered with the quasi-2D perovskite layer in different thicknesses under 1550 nm light illumination.

Published on 15 March 2022. Downloaded by HeFei University of Technology on 4/23/2022 1:15:50 AM.

perovskite thickness of 190 nm. Then, it declined gradually when further increasing the perovskite thickness, and reached a minimum absorption of ∼54.9% when the perovskite thickness achieved 380 nm. In addition, as shown in Fig. 3(c), the electric field distribution of the $PdTe_2$/Ge 2D/3D heterostructure with the quasi-2D perovskite ARC in varied thicknesses was simulated under 1550 nm NIR light illumination as well, based on the finite element method. Apparently, the electric field inside the heterostructure became stronger with the ARC and the strongest electric field was observed at the perovskite thickness of 190 nm, indicating a pronounced light confinement and trapping effect.[39] The simulation results implied that the quasi-2D perovskite ARC with an optimal thickness of 190 nm could effectively suppress the optical reflectance and enhance the light usage of the $PdTe_2$/Ge 2D/3D heterostructure at the NIR wavelength regime, which was also consistent well with the experimental results.

To deeply understand the influence of the light trapping effect of the quasi-2D perovskite on the device performance, we then studied the light-dependent photoresponse characteristics of the heterostructure-based NIR photodetectors without and with the ∼190 nm-thick quasi-2D perovskite ARC. Fig. S6(a) (ESI†) and Fig. 4(a) plot the *I–V* curves of the two devices under 1550 nm light illumination with various intensities. Clearly, both devices exhibited gradually strengthened photovoltaic effects, namely increased photovoltage and photocurrent, with the increasing light intensity. This was attributed to the increased concentration of photogenerated carriers under incident light with a higher intensity. Fig. 4(b) compares the extracted photovoltage and photocurrent at different bias voltages of the two devices as functions of the light intensity. As the light intensity was changed from ∼70 to ∼1566 μW cm^{-2}, the photovoltage values increased from ∼8 to ∼59 mV and from ∼10 to ∼61 mV, while the photocurrent values at zero bias rose from ∼1.55 to ∼33.13 μA, and from ∼2.89 to ∼53.35 μA for devices without and with the quasi-2D perovskite ARC, respectively. In addition, for all bias voltages, the device with the ARC exhibited a significantly higher photocurrent than the one without the ARC. For instance, at a high light intensity of ∼1566 μW cm^{-2}, the photocurrent values were ∼33.13, ∼41.13 and ∼52.27 μA for the device without the ARC, while those were ∼53.53, ∼66.95 and ∼72.37 μA for the device with the perovskite ARC, at biases of 0, −0.5 and −1.0 V, respectively. The above results confirmed that the light trapping effect of the quasi-2D perovskite ARC was effectual under different working bias conditions and under NIR light illumination with a wide light intensity range as well. It was also observed that the photocurrent increased remarkably with the increased reverse bias voltage for both devices, which could be ascribed to the following two reasons. The reverse bias brought an exterior electric field along the built-in one, which facilitated the separation and collection of photoexcited carriers. Also, the reverse bias

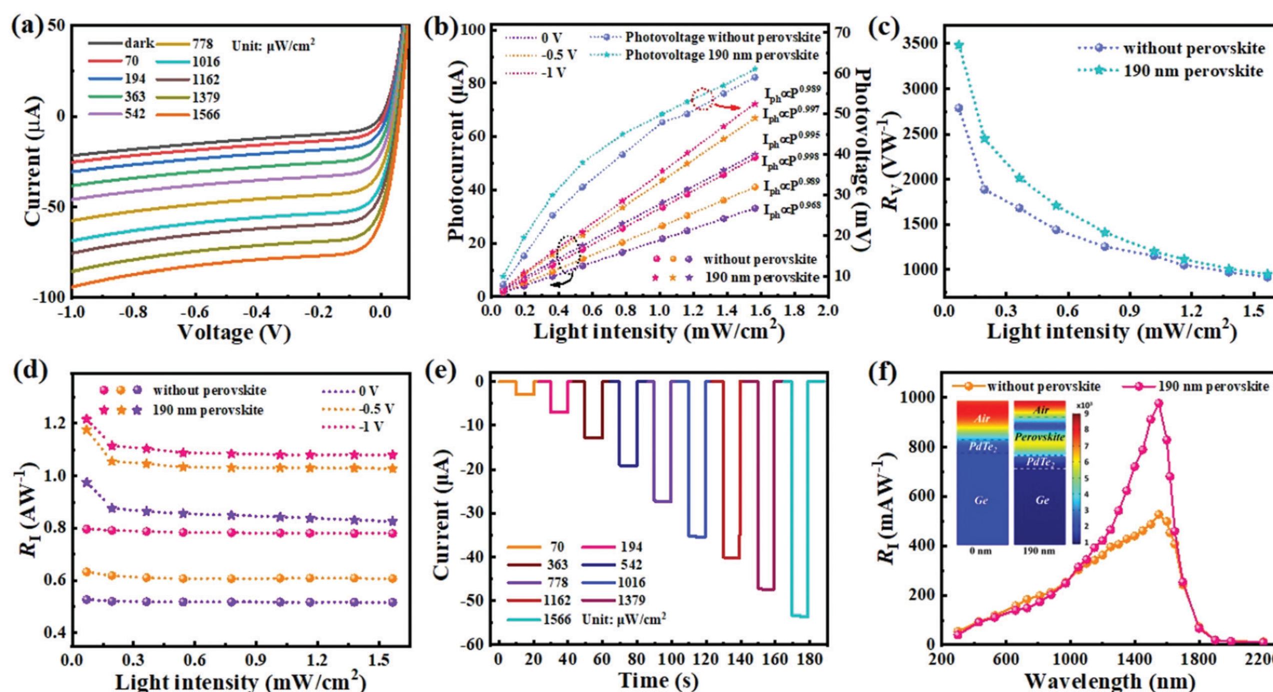

Fig. 4 *I–V* curves of the $PdTe_2$/Ge 2D/3D heterostructure-based photodetector with the perovskite ARC in the dark and under 1550 nm NIR light illuminations with various intensities. (b) Photovoltage and photocurrent at different working biases as functions of the light intensity for the conditions without and with the perovskite ARC. (c) Photovoltage responsivity and (d) photocurrent responsivity at different working biases as functions of the light intensity for the conditions without and with the perovskite ARC. (e) Time-dependent photoresponses of the device with the perovskite ARC under 1550 nm light illuminations with different intensities. (f) Photocurrent responsivity at zero bias as a function of the incident light wavelength for the conditions without and with the perovskite ARC. The inset shows the electric field distribution of the $PdTe_2$/Ge heterostructure without or with the 190 nm quasi-2D perovskite ARC under 700 nm light illumination.

This journal is © The Royal Society of Chemistry 2022

Published on 15 March 2022. Downloaded by HeFei University of Technology on 4/23/2022 1:15:50 AM.

would extend the depletion region at the interface of the heterostructure, allowing more photocarriers to take part in the production of photocurrent. Furthermore, to elucidate the relationship between the photocurrent and incident light intensity, a general power law, $I_{ph} \propto P_{\lambda}^{\theta}$, where P_{λ} denotes the light intensity, was employed to fit the dependence of the photocurrent on the light intensity. As shown in Fig. 4(b), the value of θ was deduced to be around 0.97–0.99 at different bias voltages for two devices, which was very close to the ideal value of 1, implying a negligible recombination loss of the present photodetectors within the measured light intensity range for all measured conditions.[40]

The observed apparent photovoltage and photocurrent suggested that the present heterostructure-based photodetector could work in both photovoltage and photocurrent modes. In order to compare the device performance in a quantitative way, two critical performance parameters, *e.g.* responsivity (R) and external quantum efficiency (EQE), were then calculated according to the following formulas:[41]

$$R_V = \frac{V_{ph}}{SP_{in}} \quad (1)$$

$$R_I = \frac{I_{ph}}{SP_{in}} = \left(\frac{q\lambda}{hc}\right)\text{EQE} \quad (2)$$

where R_V/R_I, V_{ph}/I_{ph}, S, P_{in}, q, λ, h and c represent the photovoltage/photocurrent responsivity, photovoltage/photocurrent, effective device area (0.04 cm^2), input light intensity, elementary charge, light wavelength, Planck's constant, and speed of light, respectively. Accordingly, the R_V/R_I (at zero bias) value was deduced to be 2789.1 V W^{-1}/526.4 mA W^{-1} without the quasi-2D perovskite ARC and could be improved remarkably by about 25%/85% to 3486.4 V W^{-1}/976.2 mA W^{-1} with the $\sim$190 nm-thick ARC, at a low light intensity of $\sim$70 μW cm^{-2}. Of note, the R_I value of 976.2 mA W^{-1} was obviously superior to previously reported NIR photodetectors made of graphene/Ge (51.8–750 mA W^{-1})[13,15,16] and other group-10 TMD/Ge (530–691 mA W^{-1})[14,17,42] and was even higher than commercial Ge NIR photodiodes (850–950 mA W^{-1}, Thorlabs series products). Fig. 4(c and d) plot the dependence of R_V and R_I at different bias voltages on the incident light intensity in the range of 70–1566 μW cm^{-2}, respectively, for two devices without and with the perovskite ARC. Apparently, the value of R_V declined gradually with the increasing light intensity, which was reasonable considering the logarithmic dependence of the photovoltage on the light intensity even in an ideal photodiode.[43] In addition, it was also observed that the value of R_I first experienced a slight decrease as the light intensity increased from $\sim$70 to $\sim$194 μW cm^{-2}, and then became nearly saturated when further increasing the light intensity to $\sim$1566 μW cm^{-2}, at all bias voltages for both devices. The result suggested that the present NIR photodetectors worked actually in their linear dynamic range, which was also in accordance with the linear dependence of photocurrents on the light intensity as above discussed. Furthermore, as displayed in Fig. 4(d), we found that the R_I value could be greatly improved by enlarging the operating bias voltage. Specifically, at a light intensity of $\sim$70 μW cm^{-2}, it increased from 526.4 to 632.2 and eventually to 796.6 mA W^{-1} and from 976.2 to 1175.7 and finally to 1216.7 mA W^{-1}, for the two devices without and with the quasi-2D perovskite ARC, respectively, when we changed working biases from 0 to −0.5 and to −1 V. Significantly, following eqn (2), the highest R_I value of 1216.7 mA W^{-1} corresponded to an EQE value of about 97.3%, which signified that nearly all incident photons were converted to electron–hole pairs, making a contribution to the photocurrent. Time-dependent photoresponse properties in Fig. S6(b) (ESI†) and Fig. 4(e) showed excellent photo-switching behaviors with rapid rise and fall edges for both devices without and with the perovskite ARC. Similarly, both photocurrents rose monotonously with the increasing light intensity as well.

In addition, the specific detectivity (D^*), which reflects the detection limit of a photodetector, is studied and it is usually given by:[44]

$$D^* = \frac{(S\Delta f)^{1/2}}{\text{NEP}} \quad (3)$$

$$\text{NEP} = \frac{\overline{i_n^2}^{1/2}}{R_I} \quad (4)$$

where NEP, Δf and $\overline{i_n^2}^{1/2}$ are the noise equivalent power, the bandwidth, and the root-mean-square value of the noise current, respectively. The $\overline{i_n^2}^{1/2}$ values at Δf = 1 Hz were deduced to be 4.33 × 10^{-13} and 4.08 × 10^{-13} A $Hz^{-1/2}$ (Fig. S7, ESI†), which rendered NEP values of 8.23 × 10^{-13} and 4.18 × 10^{-13} W $Hz^{-1/2}$, for the devices without and with the quasi-2D perovskite ARC, respectively. Accordingly, the D^* values were calculated to be about 2.43 × 10^{11} and 4.78 × 10^{11} Jones for the two devices.

Furthermore, the R_I values as functions of the incident light wavelength were recorded from 300 to 2200 nm at a constant light intensity ($\sim$70 μW cm^{-2}) for both devices without and with the perovskite ARC. Remarkably, as plotted in Fig. 4(f), both curves first increased gradually as the light wavelength was changed from 300 to 1550 nm, and then declined rapidly when further increasing the light wavelength, giving a maximum photoresponse at around 1550 nm. Upon the $\sim$190 nm-thick quansi-2D perovskite ARC, the photoresponse could be significantly improved in the wavelength range of about 1100–1650 nm. Interestingly, careful analysis found that the photoresponse even experienced somewhat decrease in the wavelength region of about 200–900 nm, which was ascribed partially to the blocking of the incident light by the quasi-2D perovskite layer as discussed later. Another reason should be the enhanced reflection effect induced by the quasi-2D perovskite film in the visible range as confirmed by the weakened electric field intensity in the $PdTe_2$/Ge heterostructure with the quasi-2D perovskite coating (the inset in Fig. 4(f)).

The above intriguing evolution in the spectrum response could be understood by analyzing the energy band diagram of the $PdTe_2$/Ge heterostructure with the quasi-2D perovskite ARC. It has been reported that the quasi-2D perovskite possessed a

Published on 15 March 2022. Downloaded by HeFei University of Technology on 4/23/2022 1:15:50 AM.

gradient type-II band alignment, and the values of the highest occupied molecular orbital (HOMO) and lowest unoccupied molecular orbital (LUMO) for $(PEA)_2(MA)_{n-1}Pb_nI_{3n+1}$ perovskites with different n values were obtained from literature studies.[24] In addition, the work function (W_f) of the $PdTe_2$ multilayer was about −4.8 eV,[22] and the values of the conduction band minimum (E_c), Fermi level (E_f) and vacuum band maximum (E_v) for n-type Ge with a resistivity of 0.1–6 Ω cm were about −4.13, −4.37 and −4.81 eV, respectively. Fig. 5(a) illustrates the energy band diagram and corresponding charge carrier transport under light illuminations. Due to the difference in the work function of two materials, a built-in electric field was constructed at the interface of the $PdTe_2$/Ge heterostructure. When the heterostructure was shinned by light illumination with the photon energy exceeding the bandgap of Ge (∼0.67 eV), photon absorption by Ge would generate electron–hole pairs, which were rapidly separated towards opposite directions by the built-in electric field. Subsequently, the holes transported across the $PdTe_2$ layer and reached the top Au electrode, while the electrons walked through the Ge substrate and were collected by the bottom In–Ga electrode, giving the production of the photocurrent. Of note, upon UV or visible light illuminations, photon absorption took place in the quasi-2D perovskite as well. The gradient band alignment could drive the separation of photoexcited electrons and holes. As shown in Fig. 5(a), the electrons and holes would accumulate at the large-n perovskite phase (bottom surface) and small-n perovskite phase (upper surface), respectively. However, since there was no conductive path, these photocarriers could not be extracted to generate the photocurrent. In contrast, photon absorption in the quasi-2D perovskite would reduce the usage of the incident light in the $PdTe_2$/Ge heterostructure, leading to a reduced photocurrent in the UV-visible wavelength region.

The response speed, as a pivotal performance parameter reflecting a device to follow a rapidly varying optical signal, was also explored. Fig. S8(a and b) (ESI†) plot the temporal photoresponse of the device with the ∼190 nm-thick perovskite ARC to 1550 nm light illumination with different modulating frequencies. Remarkably, as the frequency was changed from 0.5 to 9 kHz, the NIR photodetector could display a stable, reversible and reproducible photo-switching characteristic, showing that it operated well under these conditions. The relative balance $(V_{max} - V_{min})/V_{max}$ as a function of the modulating frequency is summarized in Fig. S8(c) (ESI†), which demonstrated a relatively slow decay. From this curve, the −3 dB frequency, the frequency at which point the photoresponse declined to 0.707 of its peak value, was deduced to be ∼9.1 kHz. Furthermore, the response times were estimated from an individual enlarged response curve recorded at a frequency of 9 kHz, as displayed in Fig. 5(b). According to their definitions,[41] the rise/fall times were calculated to be 33.5/40.5 μs and 35.9/40.7 μs for the devices without and with the ∼190 nm perovskite ARC, respectively. The fast response speeds were comparable to many previously reported 2D materials-based NIR photodetectors,[10,45] and also implied that the upper quasi-2D perovskite coating had a negligible influence on the rapid separation and transportation of photocarriers by the strong built-in electric field in the present NIR photodetector.

The advantage of our heterostructure photodetector with the quasi-2D perovskite ARC also lies in its excellent long-term ambient stability and operational durability. Fig. 6(a) plots the evolution of the normalized photocurrent of the device placed under air conditions without any encapsulation as a function of storage day, along with that of a control device with the $MAPbI_3$ 3D perovskite ARC for comparison. Fig. 6(b and c) compare the temporal photoresponses of both devices before and after 30 days storage. Significantly, after 30 days of storage, the device with the quasi-2D perovskite ARC could still maintain ∼96.3% of its initial photocurrent with well-preserved photo-switching characteristics. In contrast, the photocurrent of the device with the 3D perovskite ARC decreased remarkably to ∼71.8% of its initial value. In addition, Fig. 6(d) and Fig. S9 (ESI†) present the temporal photoresponse of the device after over 1200 cycles of operation, indicating negligible degradation in photo-switching properties. Such good air stability and durability could be attributed to the excellent intrinsic chemical

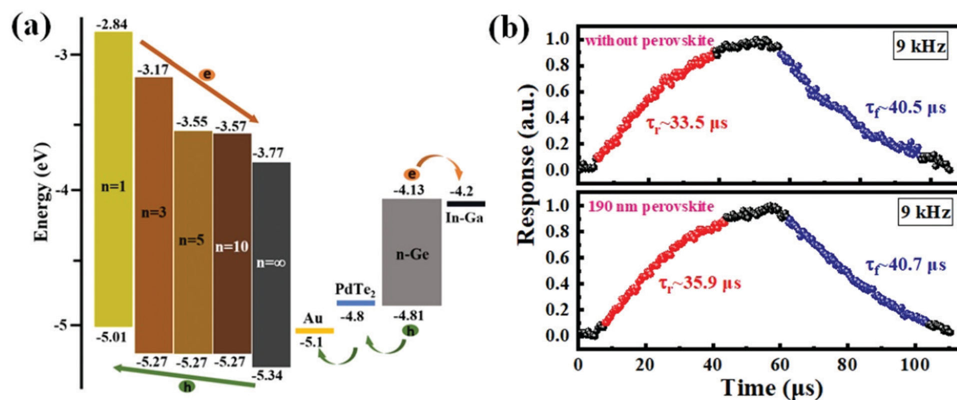

Fig. 5 (a) Energy band diagram and charge carrier transport of the $PdTe_2$/Ge 2D/3D heterostructure with the quasi-2D perovskite ARC under light illuminations. (b) An individual enlarged response curve at a modulating frequency of 9 kHz for estimating the response speed, for the conditions without (the top panel) and with the perovskite ARC (the bottom panel).

This journal is © The Royal Society of Chemistry 2022

Published on 15 March 2022. Downloaded by HeFei University of Technology on 4/23/2022 1:15:50 AM.

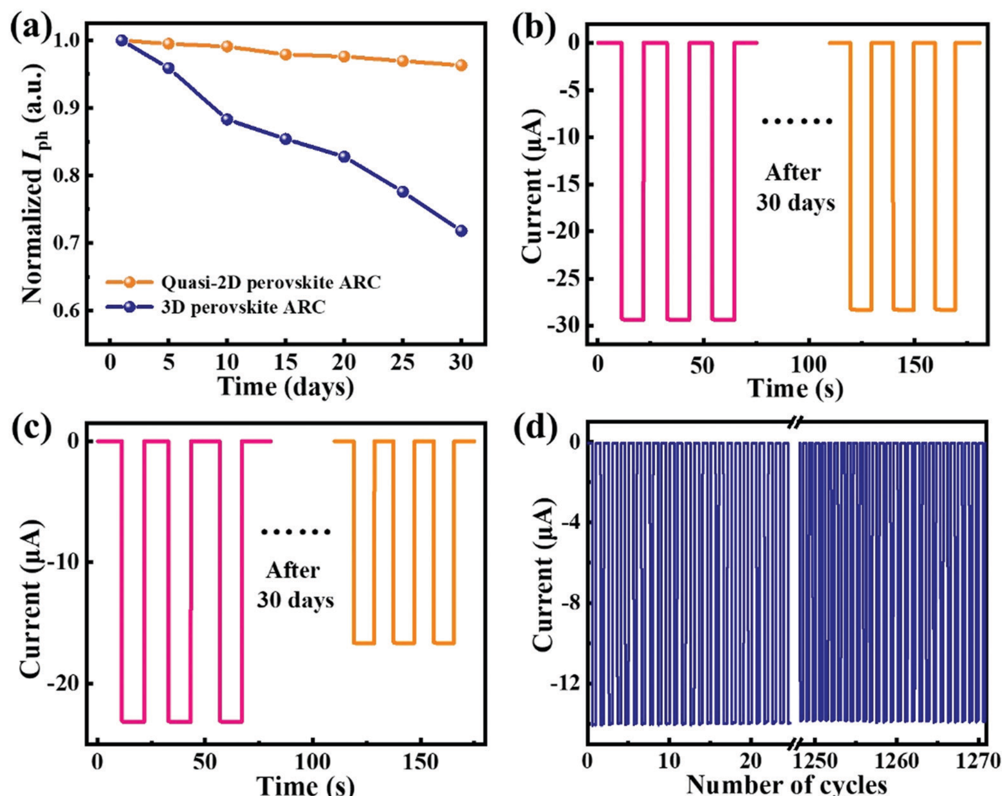

Fig. 6 (a) Evolution of the normalized photocurrent of the $PdTe_2$/Ge heterostructure-based photodetector with the quasi-2D perovskite or 3D perovskite ARC as a function of storage day. Time-dependent photoresponses of the device with the (b) quasi-2D perovskite and (c) 3D perovskite ARC before and after storage under ambient conditions for 30 days. (d) Time-dependent photoresponse of the $PdTe_2$/Ge-heterostructure-based photodetector with the quasi-2D perovskite ARC during operation over 1200 cycles.

stability of the quasi-2D perovskite and 2D $PdTe_2$ multilayer,[22,25] as well as the relatively thick layers (the quasi-2D perovskite and $PdTe_2$) that could effectively impede the oxidation at the $PdTe_2$/Ge interface.

Conclusions

In summary, we have demonstrated that an ARC of the quasi-2D perovskite thin film could significantly improve the NIR photoresponse performance of a multilayered $PdTe_2$/Ge heterostructure-based photodetector. With the optimized ARC thickness, the photocurrent responsivity and specific detectivity of the device were greatly enhanced from $\sim$526.4 mA W^{-1} to $\sim$976.2 mA W^{-1} and from $\sim 2.43 \times 10^{11}$ Jones to $\sim 4.78 \times 10^{11}$ Jones, respectively, while other performance parameters were almost unaffected, when shinned under 1550 nm NIR light illumination (light intensity: $\sim$70 μW cm^{-2}). The improvement was attributed to the strong NIR light trapping effect of the quasi-2D perovskite ARC. In addition, thanks to the enhanced moisture resistance of the upper quasi-2D perovskite layer, the device possessed excellent air stability and long-term operational durability. It was expected that the present study would offer a facile avenue for designing cost-effective highly efficient NIR optoelectronic devices, as well as expand the application field of perovskite materials.

Experimental section

Material preparation and characterization

A thermal-aided conversion method was employed to grow the 2D $PdTe_2$ multilayer according to our previous study.[22] Firstly, a $\sim$8 nm-thick Pd thin film was deposited onto a Si oxide substrate *via* an electron beam evaporation technique. Then, the substrate was laid in the central zone of a high-temperature tube furnace, and Te powder in 99.99% purity was placed at the upstream side about 10 cm away from the substrate. The temperature of the zone where the powder was placed was set to 200 °C to ensure evaporation, and 100 sccm Ar gas was used to drag the evaporated gas towards downstream. At the same time, the central zone of the tube furnace was heated to 300 °C to allow tellurization. After about 1 hour, the 2D $PdTe_2$ multilayer can be obtained on the substrate. The quasi-2D perovskite film was obtained *via* a two-step ligand exchange spin-coating method following a previous work.[25] The precursor solution of the $MAPbI_3$ 3D perovskite was acquired by dissolving 159 mg of MAI and 461 mg of PbI_2 into a mixed solvent of 133 μL of dimethylsulfoxide (DMSO, ≥99.9%) and 1867 μL of *N*,*N*-

Published on 15 March 2022. Downloaded by HeFei University of Technology on 4/23/2022 1:15:50 AM.

dimethylformamide (DMF, 99.8%), while that of the $(PEA)_2PbI_3$ 2D perovskite was obtained by dissolving 498 mg of PEAI and 461 mg of PbI_2 into a solvent of 2 mL of *N*,*N*-dimethylformamide (DMF, 99.8%). At the first step, 20 μL of the 3D perovskite precursor solution, pre-heated at 100 °C, was spin-coated on the substrate at 3000 rpm for 30 s. Then, the substate was annealed at 100 °C for about 30 s. After annealing, 20 μL of the 2D perovskite precursor solution, pre-heated at 100 °C, was dripped on the substrate spinning at 4000 rpm for 30 s as the second step. After spin-coating, the substrate was annealed at 100 °C for 30 min. With the help of thermal energy action, the 3D perovskite component would diffuse into the 2D perovskite component, generating the quasi-2D perovskite with graded multiple phases in the vertical direction.

The morphology of the product was observed using a SEM (Hitachi, SU8020). An AFM (Benyuan NanotechCom, CSPM-4000) was employed to examine the topography and height profile. The XRD pattern was recorded using an X-ray diffractometer (Rigaku D/max-rB). The Raman spectra were recorded using an HR Evolution Raman spectrometer (Horiba Jobin Yvon) equipped with a 488 nm argon-ion laser. The absorption spectrum was characterized using a Shimadzu UV-2550 UV-vis spectrophotometer. The PL spectra was explored using a confocal laser Raman spectrometer (Horiba Jobin Yvon, Labram HR evolution). The refractive index and extinction coefficient of the quasi-2D perovskite film and $PdTe_2$ multilayer were measured using an ellipsometer (J. A. Woollam, RC2 UI).

Device fabrication and analysis

The $PdTe_2$/Ge heterostructure-based photodetector with the quasi-2D perovskite ARC was fabricated by the following steps. First, ∼80 nm Al_2O_3 serving as an insulating layer was deposited onto a cleaned n-type Ge substrate (resistivity: 0.1–6 Ω cm) by using the atomic layer deposition technique. Then, an open window (0.04 cm^2) was defined on the substrate with the assistance of photolithography, and the insulating layer within the window area was removed using a wet etching procedure. After this, with the help of a shadow mask, ∼50 nm-thick Au acting as the top electrode was deposited on the insulating layer *via* high-vacuum electron beam evaporation. Subsequently, the $PdTe_2$ multilayer was transferred atop the substrate using a PMMA-assistant transfer method. Then, the quasi-2D perovskite ARC was deposited atop the $PdTe_2$ multilayer by using the aforementioned method. Finally, In–Ga alloy serving as the bottom electrode was attached to the rear side of the substrate.

Electrical characterization of the photodetector was performed using a Keithley 4200-SCS semiconductor analyzer. Light emitting diodes (LEDs, Thorlabs products) with different wavelengths were used as light sources. For the response speed study, the LED was powered with a signal generator (Tektronix, TDS2022B) to produce the pulsed light signal with varied frequencies, and an oscilloscope (Tektronix, TDS2012B) was employed to record the output electrical signal. The intensity of all light sources was carefully calibrated using a power meter (Thorlabs GmbH., PM 100D) prior to use. All measurements were performed under ambient conditions at room temperature.

Theoretical simulation

The electrical field distribution and absorbance of the $PdTe_2$/Ge heterostructure-based photodetector with the quasi-2D perovskite ARC of varied thicknesses were simulated by COMSOL. The thicknesses of the $PdTe_2$ and Ge heterostructures were set to be 58 nm and 200 μm, respectively. The designed structure was covered by a semi-infinite air layer with a permittivity of 1. The optical constants of the quasi-2D perovskite and $PdTe_2$ were obtained from the measured data (Fig. S5, ESI†) and those of the Ge were acquired from the data library of the software.

Conflicts of interest

There are no conflicts to declare.

Acknowledgements

This work was financially supported by the National Natural Science Foundation of China (NSFC, No. 51902078, 62074048, and 61675062), the Anhui Provincial Natural Science Foundation (2008085MF205), and the Fundamental Research Funds for the Central Universities (JZ2020HGTB0051, PA2020GDKC0014, and JZ2018HGPB0275). The authors acknowledge Mr Huirong Su from Genuine Optronics Ltd for providing measurements of optical constants and corresponding data analysis.

References

1 G. Konstantatos, I. Howard, A. Fischer, S. Hoogland, J. Clifford, E. Klem, L. Levina and E. H. Sargent, *Nature*, 2006, **442**, 180–183.
2 P. Martyniuk, J. Antoszewski, M. Martyniuk, L. Faraone and A. Rogalski, *Appl. Phys. Rev.*, 2014, **1**, 041102.
3 J. Li, L. Niu, Z. Zheng and F. Yan, *Adv. Mater.*, 2014, **26**, 5239–5273.
4 G. Rao, X. Wang, Y. Wang, P. Wangyang, C. Yan, J. Chu, L. Xue, C. Gong, J. Huang, J. Xiong and Y. Li, *InfoMat*, 2019, **1**, 272–288.
5 C. Xie and F. Yan, *Small*, 2017, **13**, 1701822.
6 H. C. Ko, M. P. Stoykovich, J. Song, V. Malyarchuk, W. M. Choi, C. J. Yu, J. B. Geddes 3rd, J. Xiao, S. Wang, Y. Huang and J. A. Rogers, *Nature*, 2008, **454**, 748–753.
7 C. Liu, J. Guo, L. Yu, J. Li, M. Zhang, H. Li, Y. Shi and D. Dai, *Light: Sci. Appl.*, 2021, **10**, 123.
8 Y. Wang, K. Ding, B. Sun, S.-T. Lee and J. Jie, *Nano Res.*, 2016, **9**, 72–93.
9 C. Xie, Y. Wang, Z. X. Zhang, D. Wang and L. B. Luo, *Nano Today*, 2018, **19**, 41–83.
10 M. Long, P. Wang, H. Fang and W. Hu, *Adv. Funct. Mater.*, 2019, **29**, 1803807.
11 M. Zhao, Z. Xue, W. Zhu, G. Wang, S. Tang, Z. Liu, Q. Guo, D. Chen, P. K. Chu, G. Ding and Z. Di, *ACS Appl. Mater. Interfaces*, 2020, **12**, 15606–15614.

This journal is © The Royal Society of Chemistry 2022

View Article Online

Published on 15 March 2022. Downloaded by HeFei University of Technology on 4/23/2022 1:15:50 AM.

12 J. Wu, Z. Yang, C. Qiu, Y. Zhang, Z. Wu, J. Yang, Y. Lu, J. Li, D. Yang, R. Hao, E. Li, G. Yu and S. Lin, *Nanoscale*, 2018, **10**, 8023–8030.

13 L.-H. Zeng, M.-Z. Wang, H. Hu, B. Nie, Y.-Q. Yu, C.-Y. Wu, L. Wang, J.-G. Hu, C. Xie, F.-X. Liang and L.-B. Luo, *ACS Appl. Mater. Interfaces*, 2013, **5**, 9362–9366.

14 L. Wang, J.-J. Li, Q. Fan, Z.-F. Huang, Y.-C. Lu, C. Xie, C.-Y. Wu and L.-B. Luo, *J. Mater. Chem. C*, 2019, **7**, 5019–5027.

15 K. E. Chang, C. Kim, T. J. Yoo, M. G. Kwon, S. Heo, S. Kim, Y. Hyun, J. Il Yoo, H. C. Ko and B. H. Lee, *Adv. Electron. Mater.*, 2019, **5**, 1800957.

16 R. Lu, C.-W. Ge, Y.-F. Zou, K. Zheng, D.-D. Wang, T.-F. Zhang and L.-B. Luo, *Laser Photon. Rev.*, 2016, **10**, 595–602.

17 L. Luo, D. Wang, C. Xie, J. Hu, X. Zhao and F. Liang, *Adv. Funct. Mater.*, 2019, **29**, 1900849.

18 E. Shi, H. Li, L. Yang, L. Zhang, Z. Li, P. Li, Y. Shang, S. Wu, X. Li, J. Wei, K. Wang, H. Zhu, D. Wu, Y. Fang and A. Cao, *Nano Lett.*, 2013, **13**, 1776–1781.

19 X. Gan, R. Lv, H. Zhu, L.-P. Ma, X. Wang, Z. Zhang, Z.-H. Huang, H. Zhu, W. Ren, M. Terrones and F. Kang, *J. Mater. Chem. A*, 2016, **4**, 13795–13802.

20 F. Zhang, H. Lu, J. Tong, J. J. Berry, M. C. Beard and K. Zhu, *Energy Environ. Sci.*, 2020, **13**, 1154–1186.

21 C. Xie, C. Liu, H. Loi and F. Yan, *Adv. Funct. Mater.*, 2020, **30**, 1903907.

22 Y. Liang, C. Xie, C. Dong, X. Tong, W. Yang, C. Wu and L. Luo, *J. Mater. Chem. C*, 2021, **9**, 14897–14907.

23 E. Li, R.-Z. Zhang, H. Li, C. Liu, G. Li, J.-O. Wang, T. Qian, H. Ding, Y.-Y. Zhang, S.-X. Du, X. Lin and H.-J. Gao, *Chin. Phys. B*, 2018, **27**, 086804.

24 S. Wei, F. Wang, X. Zou, L. Wang, C. Liu, X. Liu, W. Hu, Z. Fan, J. C. Ho and L. Liao, *Adv. Mater.*, 2020, **32**, 1907527.

25 Y. Shao, Y. Liu, X. Chen, C. Chen, I. Sarpkaya, Z. Chen, Y. Fang, J. Kong, K. Watanabe, T. Taniguchi, A. Taylor, J. Huang and F. Xia, *Nano Lett.*, 2017, **17**, 7330–7338.

26 J. Jiang, X. Zou, Y. Lv, Y. Liu, W. Xu, Q. Tao, Y. Chai and L. Liao, *Nat. Commun.*, 2020, **11**, 4266.

27 H. Loi, J. Cao, X. Guo, C. Liu, N. Wang, J. Song, G. Tang, Y. Zhu and F. Yan, *Adv. Sci.*, 2020, **7**, 2000776.

28 C. Yim, N. McEvoy, S. Riazimehr, D. S. Schneider, F. Gity, S. Monaghan, P. K. Hurley, M. C. Lemme and G. S. Duesberg, *Nano Lett.*, 2018, **18**, 1794–1800.

29 E. Wu, D. Wu, C. Jia, Y. Wang, H. Yuan, L. Zeng, T. Xu, Z. Shi, Y. Tian and X. Li, *ACS Photonics*, 2019, **6**, 565–572.

30 L. Wang, J. Jie, Z. Shao, Q. Zhang, X. Zhang, Y. Wang, Z. Sun and S.-T. Lee, *Adv. Funct. Mater.*, 2015, **25**, 2910–2919.

31 L.-B. Luo, J.-J. Chen, M.-Z. Wang, H. Hu, C.-Y. Wu, Q. Li, L. Wang, J.-A. Huang and F.-X. Liang, *Adv. Funct. Mater.*, 2014, **24**, 2794–2800.

32 X. An, F. Liu, Y. J. Jung and S. Kar, *Nano Lett.*, 2013, **13**, 909–916.

33 K. Yu, F. Yang, H. Cong, L. Zhou, Q. Liu, L. Zhang, B. Cheng, C. Xue, Y. Zuo and C. Li, *J. Alloys Compd.*, 2018, **750**, 182–188.

34 W. Hu, H. Cong, W. Huang, Y. Huang, L. Chen, A. Pan and C. Xue, *Light: Sci. Appl.*, 2019, **8**, 106.

35 H. K. Raut, V. A. Ganesh, A. S. Nair and S. Ramakrishna, *Energy Environ. Sci.*, 2011, **4**, 3779.

36 E. Garnett and P. Yang, *Nano Lett.*, 2010, **10**, 1082–1087.

37 Z. Lai, Y. Meng, Q. Zhu, F. Wang, X. Bu, F. Li, W. Wang, C. Liu, F. Wang and J. C. Ho, *Small*, 2021, **17**, 2100442.

38 H. A. MacLeod and H. A. Macleod, *Thin-Film Optical Filters*, CRC Press, 2010.

39 B. Nie, J.-G. Hu, L.-B. Luo, C. Xie, L.-H. Zeng, P. Lv, F.-Z. Li, J.-S. Jie, M. Feng, C.-Y. Wu, Y.-Q. Yu and S.-H. Yu, *Small*, 2013, **9**, 2872–2879.

40 X. Li, M. Zhu, M. Du, Z. Lv, L. Zhang, Y. Li, Y. Yang, T. Yang, X. Li, K. Wang, H. Zhu and Y. Fang, *Small*, 2016, **12**, 595–601.

41 C. Xie, C. Mak, X. Tao and F. Yan, *Adv. Funct. Mater.*, 2017, **27**, 1603886.

42 D. Wu, J. Guo, J. Du, C. Xia, L. Zeng, Y. Tian, Z. Shi, Y. Tian, X. J. Li, Y. H. Tsang and J. Jie, *ACS Nano*, 2019, **13**, 9907–9917.

43 S. M. Sze and K. K. Ng, *Physics of Semiconductor Devices*, 2007.

44 J. D. Yao, Z. Q. Zheng and G. W. Yang, *Prog. Mater. Sci.*, 2019, **106**, 100573.

45 J. Wang, H. Fang, X. Wang, X. Chen, W. Lu and W. Hu, *Small*, 2017, **13**, 1700894.